Rock and Soil Mechanics

Volume 41 | Issue 11 Article 4

4-8-2021

Experimental study on loading rate effects of sandstone deformation localization based on 3D-DIC technology

Shou-jian PENG
State and Local Joint Engineering Laboratory of Methane Drainage in Complex Coal Gas Seam, Chongqing University, Chongqing 400044, China

Xiao-meng RAN
State and Local Joint Engineering Laboratory of Methane Drainage in Complex Coal Gas Seam, Chongqing University, Chongqing 400044, China

Jiang XU
State and Local Joint Engineering Laboratory of Methane Drainage in Complex Coal Gas Seam, Chongqing University, Chongqing 400044, China

Can-can CHEN
State and Local Joint Engineering Laboratory of Methane Drainage in Complex Coal Gas Seam, Chongqing University, Chongqing 400044, China

See next page for additional authors

Follow this and additional works at: https://rocksoilmech.researchcommons.org/journal

 Part of the Geotechnical Engineering Commons

Custom Citation

PENG Shou-jian, RAN Xiao-meng, XU Jiang, CHEN Can-can, SONG Xiao-zheng, YAN Fa-zhi, . Experimental study on loading rate effects of sandstone deformation localization based on 3D-DIC technology[J]. Rock and Soil Mechanics, 2020, 41(11): 3591-3603.

This Article is brought to you for free and open access by Rock and Soil Mechanics. It has been accepted for inclusion in Rock and Soil Mechanics by an authorized editor of Rock and Soil Mechanics.

Experimental study on loading rate effects of sandstone deformation localization based on 3D-DIC technology

Authors

Shou-jian PENG, Xiao-meng RAN, Jiang XU, Can-can CHEN, Xiao-zheng SONG, and Fa-zhi YAN

This article is available in Rock and Soil Mechanics: https://rocksoilmech.researchcommons.org/journal/vol41/iss11/4

Rock and Soil Mechanics 2020 41(11): 3591−3603 ISSN 1000−7598
https: //doi.org/10.16285/j.rsm.2020.5144 rocksoilmech.researchcommons.org/journal

Experimental study on loading rate effects of sandstone deformation localization based on 3D-DIC technology

PENG Shou-jian[1, 2], RAN Xiao-meng[1, 2], XU Jiang[1, 2], CHEN Can-can[1, 2], SONG Xiao-zheng[1, 2], YAN Fa-zhi[1, 2]

1. State Key Laboratory of Coal Mine Disaster Dynamics and Control, Chongqing University, Chongqing 400044, China
2. State and Local Joint Engineering Laboratory of Methane Drainage in Complex Coal Gas Seam, Chongqing University, Chongqing 400044, China

Abstract: The characteristics of sandstone localized deformation have been studied by visual triaxial compression servo control test system under different loading rates. By the use of the 3D-DIC (3 dimensional digital image correlation) test system, we obtain the axial and radial strain field nephogram, as well as the crack evolution process of sandstone under triaxial stress. The influence of loading rate on the localized deformation of sandstone has been analyzed. The results show that: before the peak strength, the surface deformation of sandstone is relatively uniform. The strain concentration phenomenon occurs at the peak strength, and it expands rapidly in the post-peak stage, and finally forms a deformation localized zone that penetrates the sample surface. As the load rate increases, the peak strength, elastic modulus, Poisson's ratio, peak axial strain and peak radial strain of sandstone all increase. When the loading rate increases from 1×10^{-6} s^{-1} to 1×10^{-3} s^{-1}, the starting stress of localization of deformation also increases. Besides, the ratios σ_A / σ_{peak} and σ_R / σ_{peak}, which describe the levels of the starting stress of axial and radial deformation localization, have changed from 92.00% and 93.75% after the peak to 97.17% and 96.00% before the peak, respectively, indicating that the deformation localization of sandstone has relatively obvious loading rate effects.

Keywords: sandstone; 3D-DIC; strain field nephogram; deformation localization; rate effect

1 Introduction

When the stress on the mine rock exceeds the capacity of the surrounding rock itself, it will cause the instability and destruction of the surrounding rock mass, which then affects the safety of the underground stope. In most cases, the instability and destruction of rocks are caused by the development of deformation localization [1–3]. Therefore, it is important to study the instable and destructive process of rocks from the perspective of deformation localization, which can open up great potential in order to improve the stability of underground spatial structures.

Deformation localization of materials such as rocks has been extensively studied by researchers around the world. Song et al. [4] carried out the uniaxial compression test of red sandstone under different loading rates. Based on the digital speckle correlation method, they showed that the starting stress of rock deformation localization increased with loading rate and gradually approached the peak strength. Dong et al. [5] used the GCTS electro-hydraulic servo control triaxial testing system to serve the temperature and pressure control. They conducted the triaxial tests of constant axial pressure and unloading confining pressure under freezing (10 ℃) conditions, in order to simulate the stress change of surrounding rock during wellbore excavation and therefore investigate the deformation characteristics of frozen sandstone. Yin et al. [6] employed numerical tests of uniaxial compression to study the effect of loading rate on the failure of rock surface, and found that with the increase of loading rate, the extent of destructed rock also increased, and the destruction has been developing gradually from local to global. Wang [7] used FLAC to simulate the shear zone and deformation characteristics of rocks at different loading rates, and showed that as the loading rate increases, the rock sample changed gradually from single shear failure to X-shaped shear failure. Wang et al.[8] applied the white-light digital speckle correlation method to obtain the data describing the time evolution of rock deformation localization during the entire loading process, and found that the localized zone on the rock surface developed along the direction of the maximum principal strain. Sun et al. [9] performed uniaxial compression tests of marble, and by using the digital speckle correlation method, they investigated the localization process of the surface deformation of the rock after freeze-thaw corrosion. Li et al. [10] developed a rock mechanics program that can construct mesh-free numerical models, and by using the Mohr-Coulomb criterion they showed the localized evolution process of the deformation of defected rocks. Tuong et al. [11] and Zhao et al. [12] showed the study of the displacement field, global strain field and crack evolution of rock specimens with pre-fabricated cracks during loading process. Dewers et al. [13] applied symmetric compression

Received: 9 Janury 2020 Revised: 13 April 2020
This work was supported by the National Natural Science Foundation of China (51874055, 51974041) and the Basic and Frontier Research Projects of Chongqing (cstc2018jcyjAX0626)
First: PENG Shou-jian, male, born in 1983, Phd, Associate Professor, Research interests: Mine rock mechanics, coal and gas outburst disaster dynamics and control. E-mail: sjpeng@cqu.edu.cn

on porous sandstone, and analyzed the strain localization during deformation. Bésuelle et al. [14] examined the effects of confining pressure on the properties of Vosges sandstone, as well as its local deformation characteristics during failure.

Digital image correlation (DIC) method has been applied extensively to the study of rock deformation and failure. Munoz et al. [15] used the 3D-DIC method to monitor the entire evolution of the stress–strain variation as well as the shear strain field of rock under uniaxial compression. Dautria et al. [16] and Yang et al. [17] applied the DIC technique to the study of non-uniform deformation and tensile strain of carbonates and granites. Aliabadian et al. [18] and Sharafifisafa et al. [19] used the DIC method to respectively study the crack initiation and propagation process of sandstone disc and 3D printed rock samples by applying Brazil split test. Huang et al.[20] used the DIC technique to study the shear deformation of five types of reinforced concrete. Tang et al.[21] carried out uniaxial and triaxial compression tests on the testing rocks, and by using the DIC technique they obtained the cloud diagram of the principal strain field of the rock as well as the evolution of cracks in 3D. Zhou et al. [22] applied the DIC method to studying the fracture behavior of brittle and ductile rocks under uniaxial loading. Xing et al.[23] used high-speed, 3D–DIC technique to study the full-field strain of rock materials under dynamic loading conditions. The results showed that the strain localization initiated from the surface of the sample, and evolved following the tension, shear and perpendicular direction in order. Yang et al.[24] used the DIC technique to study the displacement evolution of rock deformation localization under a constant-amplitude, cyclic loading condition.

Conventional pressure chambers are mostly made of metal materials in order to meet the requirements of triaxial tests under high confining pressure. They often cannot be used to achieve visual monitoring of the deformation and failure process of rocks. As a result, most of the studies on rock deformation localization are based on uniaxial compressional condition. There are still limited studies on the evolution of rock surface deformation localization under triaxial compression. It is still not fully clear how the localization of rock deformation changes with different loading rates. This study was based on a visual triaxial compression servo testing system, as well as a 3D-DIC testing system to carry out triaxial compression tests on sandstone samples under different loading rates. By monitoring the whole process of rock deformation and failure using the 3D-DIC system, we analyzed the evolution process of the rock deformation on the surface of samples, and discussed the effects of loading rate on the rock mechanical properties, as well as the threshold of the starting stress for a deformation localization.

2 Experiments

2.1 Sample collection and preparation

The sandstone samples used in the test are collected from the Xujiahe Formation of the Upper Triassic in Jingkou Town, Chongqing, China, and they belong to terrigenous fine-grained clastic sedimentary rocks. The particle size is between 0.1 and 0.5 mm, and the minerals mainly consist of quartz, feldspar, dolomite and flint. All the rock samples are collected by taking cores from the rock blocks in the direction perpendicular to the bedding. According to the standards by International Society for Rock Mechanics and Rock Engineering (ISRM), the surfaces of the samples are polished to ensure the flatness of the end surfaces, and all the samples are processed into a uniform cylindrical shape with a diameter of 25 mm and a height of 50 mm. By spraying white and black paints on the surface, we obtained speckle sandstone specimens as shown in Fig. 1. The resultant sandstone sample has a uniaxial compressive strength of 48.30 MPa, an elastic modulus of 10.57 GPa, a Poisson's ratio of 0.45 and a density of 2.40 g/cm^3.

(a) Sandstone specimens

(b) Speckled sandstone specimens

Fig. 1 Speckled sandstone specimens

2.2 Experimental device

The device used in the experiment was a visual triaxial compression servo control test system [26], with the maximum axial load of 500 kN, the maximum axial displacement of 10 mm, the maximum confining pressure of 10 MPa, and a rigidity of the test bench of 5 GN/m. The displacement speed can be controlled from 0.00001–300 mm/min. There are three methods of loading: displacement load, force load, and a combina-

tion of displacement and force load. Figure 2 shows a photo of the transparent pressure chamber. The key part is the middle-part, transparent cylinder made of acrylic resin polymer material, which can be used to achieve the visual observation of deformation and failure process of the rock samples during the experiments.

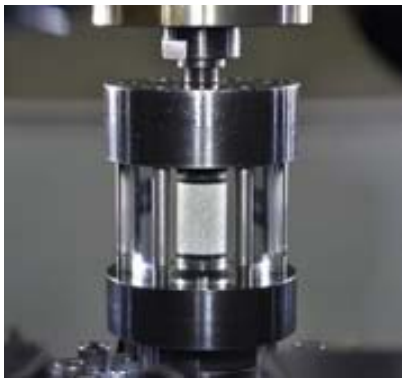

Fig. 2 Transparent pressure chamber

The 3D-DIC system [27] used in this experiment mainly consists of a hardware system for image acquisition and a software system for image processing. There are in total 6 cameras in the hardware system, which are divided into 3 groups in order to acquire images in 3D, namely L1, L2, and L3, and they surround the transparent pressure chamber evenly. Figure 3 gives a schematic diagram of the camera layout.

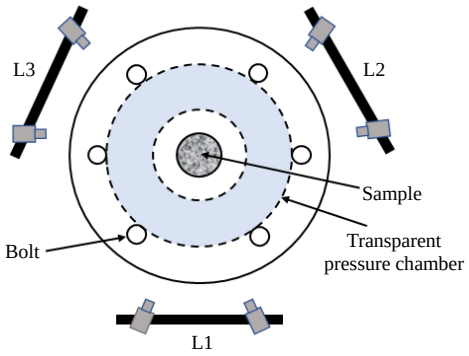

Fig. 3 Schematic diagram of camera layout

The 3D-DIC can achieve the visual monitoring of the full-field deformation, local deformation and the evolution of the deformation localization of the sandstone surface under triaxial compression condition. Nevertheless, due to the limitation of the cavity space of the triaxial pressure chamber, it is still not capable to obtain a full 360° view of the crack propagation process on the surface of rock samples. Figure 4 shows the visual triaxial compression servo control test system and the 3D-DIC test system.

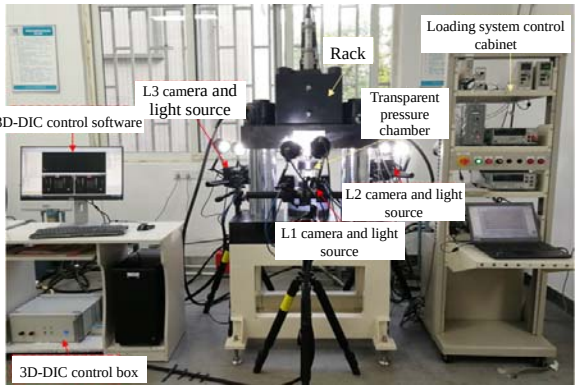

Fig. 4 Visual triaxial compression servo control testing system and 3D-DIC observation system

2.3 Design and parameters

We carried out the triaxial compression test with the specified sandstone samples. During the test, the confining pressure was fixed to 3 MPa, and the loading rates are 10^{-6}, 10^{-5}, 10^{-4} and 10^{-3} s^{-1}, respectively. The tests were repeated 3 times for each testing condition. The specific design and parameters are listed in Table 1.

Table 1 Experiments and parameters

Lithology	Water bearing state	Confining pressure / MPa	Loading rate / s^{-1}	Number of samples
Sandstone	Saturation	3	1×10^{-6}, 1×10^{-5}, 1×10^{-4}, 1×10^{-3}	Test 3 samples repeatedly at each rate
Sandstone	Saturation	3		Test 3 samples repeatedly at each rate
Sandstone	Saturation	3		Test 3 samples repeatedly at each rate
Sandstone	Saturation	3		Test 3 samples repeatedly at each rate

3 Results and analysis

3.1 Effects of loading rate on the evolution of surface strain field

Due to the length of the paper, we show only one example to analyze the evolution process of the rock surface strain field under a loading rate of 10^{-6} s^{-1}.

Figure 5 shows the full stress-strain plots of the rock sample under triaxial compression with a loading rate of 10^{-6} s^{-1}. The symbols σ_1 and σ_3 denote axial and radial stresses, respectively, and ε_1 denotes the axial strain. For the analysis shown later, we select 7 characteristic points on the plot with respect to σ_{peak}, where σ_{peak} is the peak stress, that is: 0.80 σ_{peak} (point *a*) before the peak, which corresponds to the threshold of the expansion stress damage of the rock [28]; we also choose the point at the peak stress (point *b*), as well as the a series of factors 0.90, 0.76, 0.50, 0.40, 0.21 of σ_{peak} after the peak arrival, corresponding to points *c*, *d*, *e*, *f*, and *g*, respectively.

Under the loading rate of 10^{-6} s^{-1}, Figure 6 shows

the 3D snapshots of the axial strain field from three planar views L1, L2 and L3, collected at the seven characteristic time points that listed above.

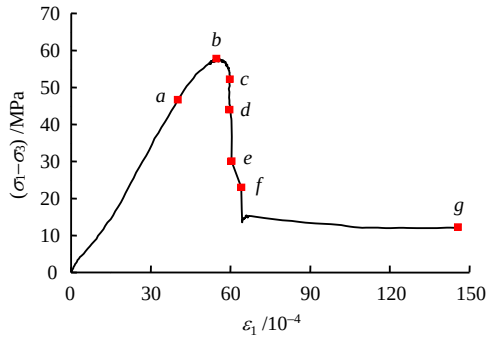

Fig. 5 Typical stress–strain plot and the characteristic marking points

As shown in Fig. 6(a), before the peak arrival, the strength of the axial strain field is relatively consistent, which means that the rock surface deformation is relatively uniform. This indicates that no penetrating cracks have formed on the rock surface before the peak stress.

As shown in Fig. 6(b), when the stress reaches the peak, the sample show a mild strain concentration on the two observation surfaces L1 and L2. It indicates that the cracks inside the rock have started to connect and gradually developed to the surface of the specimen. At the time of post-peak 0.90 σ_{peak}, the range and amplitude of the strain on the surfaces L1 and L2 both increase, whereas a mild strain concentration also appears in the upper section of surface L3, as shown in Fig. 6(c).

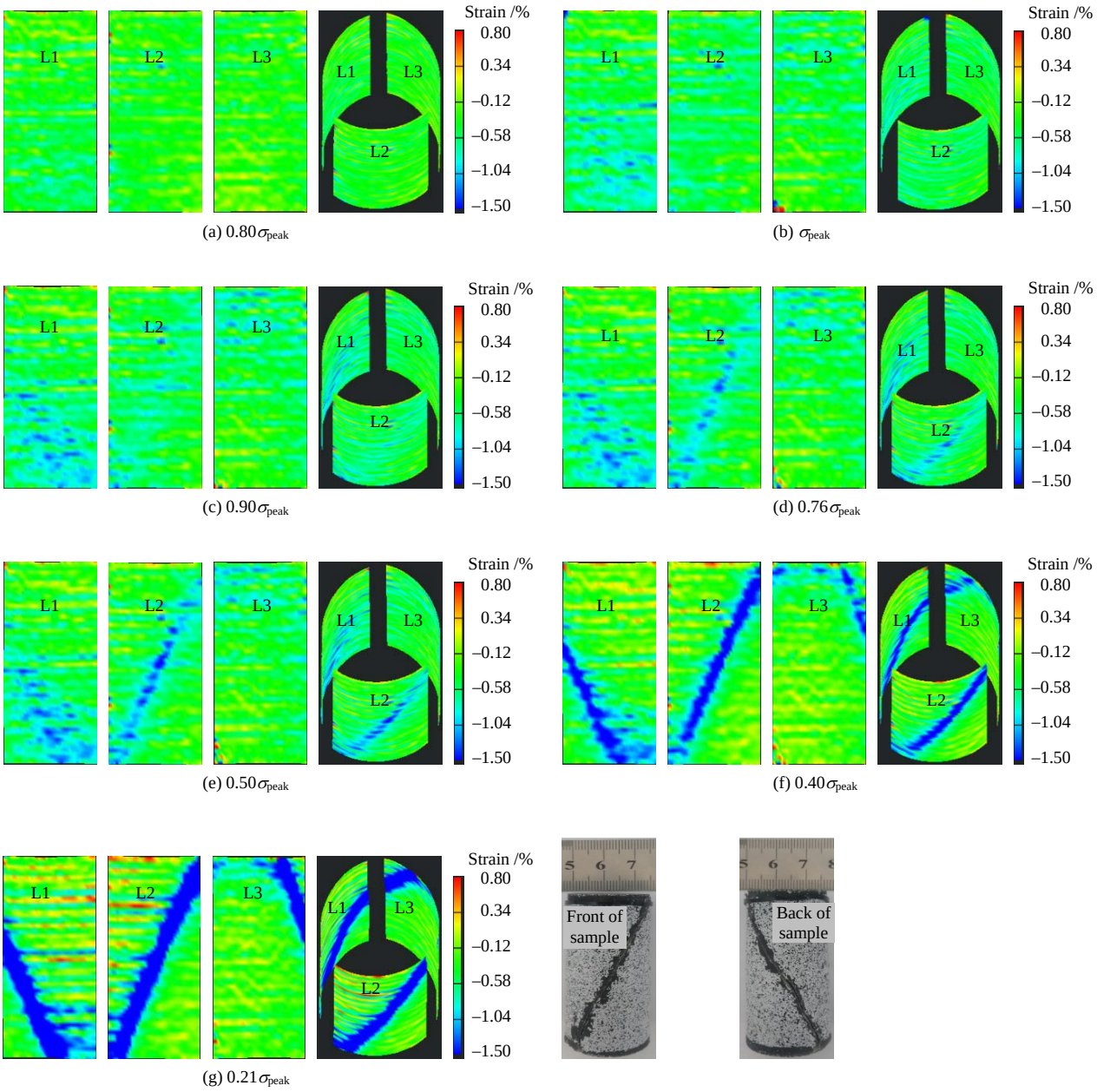

Fig. 6 Evolution of axial strain field of sandstone under different stress levels

At time positions of post-peak $0.76\,\sigma_{peak}$, $0.50\,\sigma_{peak}$, $0.40\,\sigma_{peak}$, and $0.21\,\sigma_{peak}$, localized deformation zones can be clearly observed in the lower-left section of L1, the entire section of L2 and the upper-right section of L3. The appearance of localized deformation indicates that the rock sample has developed macroscopic fractures, as shown in Fig. 6(g).

As observed from the 3D snapshots, under the triaxial compressional condition, the rock sample presents a shear failure process, and the shear cracks are developed and distributed symmetrically on the three observation surfaces L1, L2, and L3.

Figure 7 gives the snapshots of the evolution of the radial strain field of the sandstone sample at the selected 7 characteristic time points. As shown from the snapshots, before the peak arrival (Fig. 7(a)), the strength of the radial strain field is relatively consistent, which indicates the surface deformation of the rock sample is relatively uniform on the L1, L2, and L3 observation area. When the peak amplitude is reached (as shown in Figure 7(b)), there is a mild strain concentration observed in L1 and L2. At the post-peak time positions 0.90 σ_{peak} and 0.76 σ_{peak} (as shown in Figs. 7(c) and 7(d)), the strain concentration observed in L1 and L2 further develops, and a strain concentration also appears in the upper-right corner of L3. After the post-peak time $0.76\,\sigma_{peak}$ (as shown in Figs. 7(e), 7(f) and 7(g)), the strain concentration on the surface of the rock sample continues to develop, and finally forms macroscopic fracture zones on the observation surfaces L1, L2, and L3.

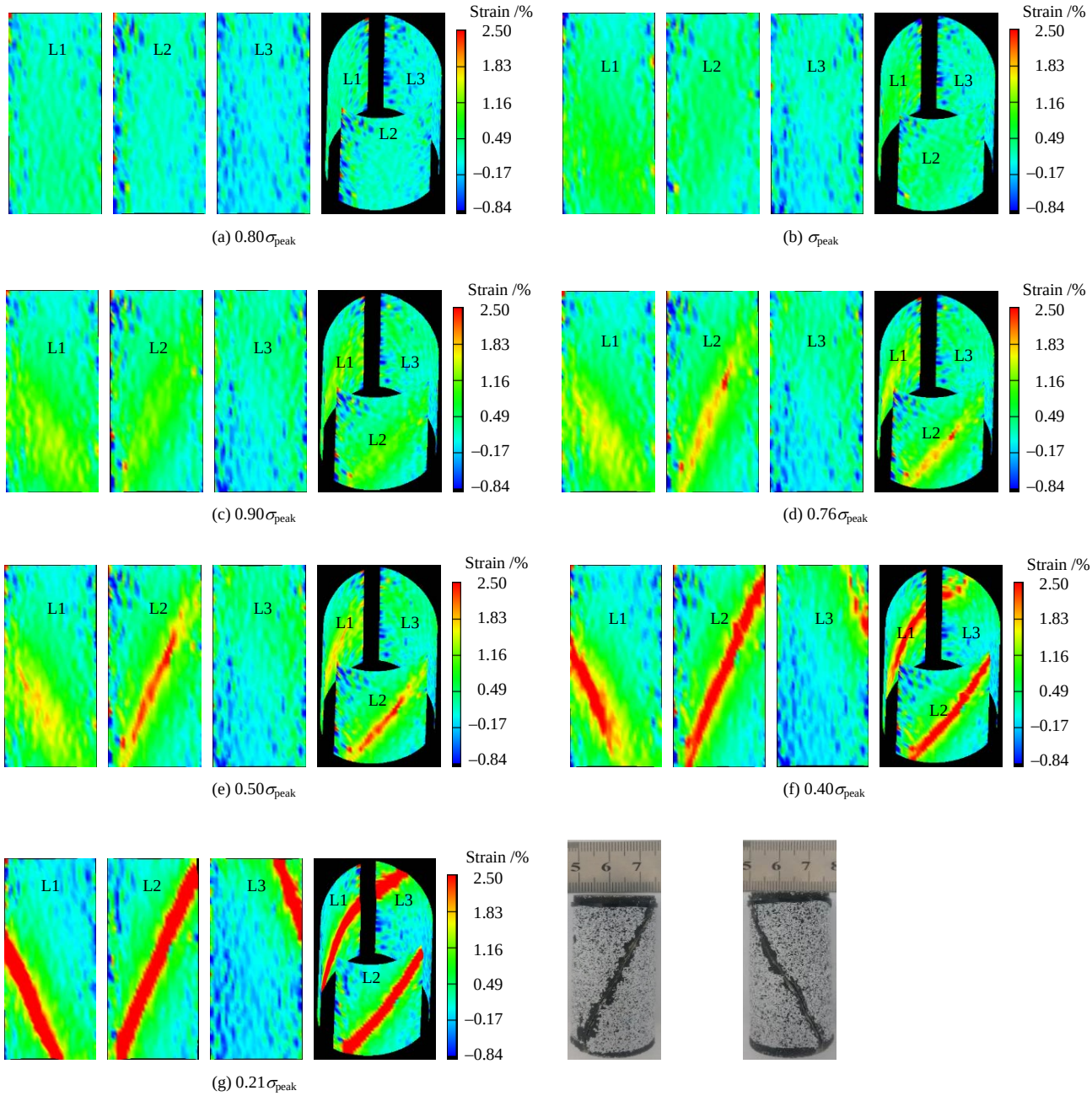

Fig. 7 Evolution of radial strain field of sandstone under different stress levels.

Figure 8 shows that under different loading rates, the snapshots of the axial and radial strain fields of the sandstone sample collected at time point *c*. Note that the colorbar is consistent for the snapshots under different loading rates. The symbol ε_3 denotes radial strain. As shown from Fig. 8, the rock samples all present shear failure under the four different loading rates. This is because that under triaxial compression, due to the presence of confining pressure, the failure of rock is mainly dominated by shear cracks[21]. At the same time, with the increase of loading rate, the deformation localization shown by the stress snapshots becomes more obvious on the surface of rocks, and therefore the non-uniform deformation of the rock surface becomes more significant.

In addition, as seen in Fig. 8, the width of the localized deformation zone shows an increasing trend with the increase of the loading rate. It indicates that the greater the loading rate, the more severe the failure of the rock sample. This is consistent with the observation discussed in recent work [4], that with the increase of loading rate, the overall sample shows an increasing trend of the extent of fragmentation and failure. This is mainly because the accumulation of energy in the pre-peak stage and the release of energy in the post-peak stage both increase with the increase of loading rate, which can lead to more thoroughly developed micro cracks near the fracture surface, as well as a more significant simultaneous sliding of multiple micro cracks through the failure process.

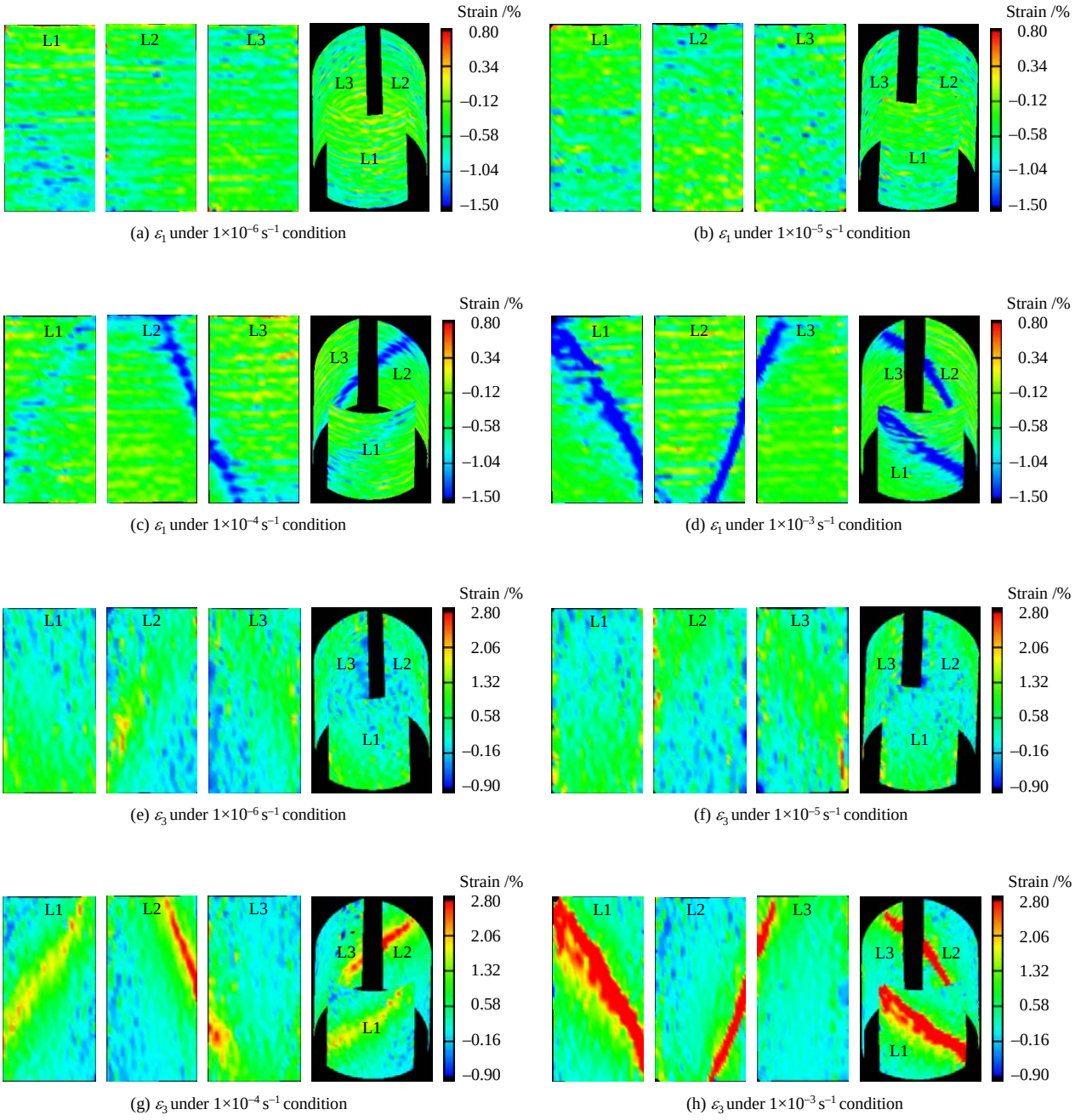

(a) ε_1 under 1×10^{-6} s^{-1} condition

(b) ε_1 under 1×10^{-5} s^{-1} condition

(c) ε_1 under 1×10^{-4} s^{-1} condition

(d) ε_1 under 1×10^{-3} s^{-1} condition

(e) ε_3 under 1×10^{-6} s^{-1} condition

(f) ε_3 under 1×10^{-5} s^{-1} condition

(g) ε_3 under 1×10^{-4} s^{-1} condition

(h) ε_3 under 1×10^{-3} s^{-1} condition

Fig. 8 Comparison of snapshots of sandstone surface deformation under different loading rates (*c* moment)

3.2 Effects of loading rate on mechanical parameters

Figure 9 shows the stress–strain plots and the variations of mechanical parameters under different loading rates.

As shown from Fig. 9(a), the stress–strain plot is concave up at the beginning of loading, which results from the initial compaction of the original pores and joints of the sample. Subsequently, because of the initial compaction, the rock exhibits linear elastic properties, and the stress–strain plot is approximately straight at this time. As the axial stress increases, the rock shows plastic deformation, and the stress–strain plot shows a convex shape. When the axial stress exceeds its maximum loading threshold, the sample starts to break and the plot shows a downward trend. The stress rises again after the sample breaks, which is due to the collapse of the pores during the failure of the sample, causing some of the cracks to close again [30]. With the increase of loading rate, the slope of the straight-line section of the stress–strain plot also increases. The peak amplitude increases as well.

It can be observed directly from Figs. 9(b) to 9(f) that the peak strength, elastic modulus, Poisson's ratio and axial strain at the peak strength of the sandstone sample all increase with the increase of loading rate, whereas the radial strain at the peak strength decreases with the increase of loading rate. It is because the greater the loading rate, the shorter the time required for rock failure occurs, so that the internal original pores and cracks do not have sufficient time to develop, which improves the ability of the rock to resist external deformation and leads to the increase of peak strength and elastic modulus. At the same time, with the increase of loading rate, there is less sufficient time between the particles in the rock to adjust their relative spatial position, which leads to the increase of anisotropy: the transverse deformation and the axial deformation show a greater difference, resulting in an increase of the Poisson's ratio of the rock.

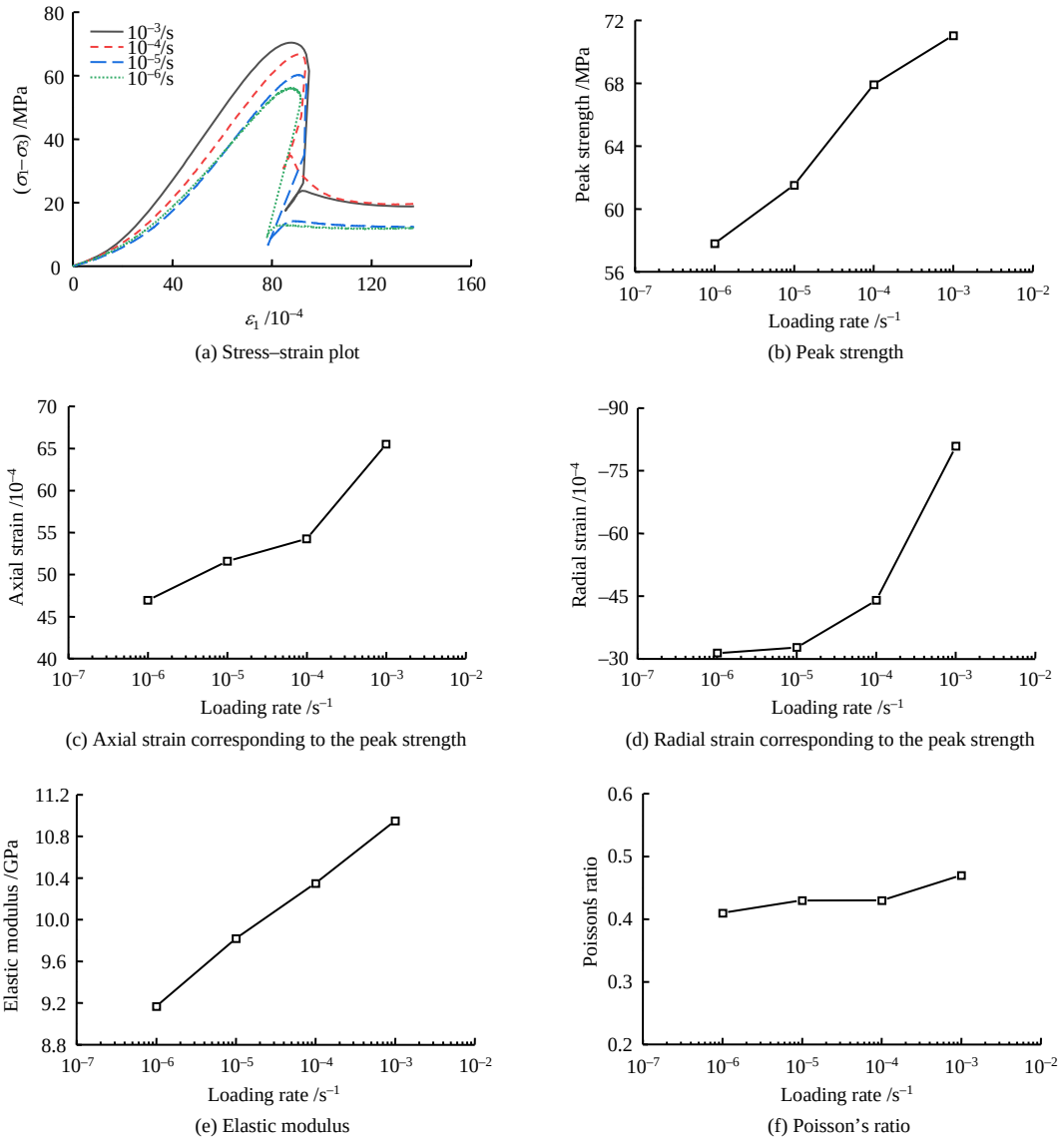

(a) Stress–strain plot

(b) Peak strength

(c) Axial strain corresponding to the peak strength

(d) Radial strain corresponding to the peak strength

(e) Elastic modulus

(f) Poisson's ratio

Fig. 9 Stress–strain plots and the variations of mechanical parameters with respect to the loading rate

In addition, when the loading rate is low, the slip and dislocation inside the rock sample converge to the main cracking area, and the time is sufficient for crack propagation. The rock sample does not need to be deformed too much until the failure by a few (or just one) dominant macroscopic cracks. In contrast, when the loading rate is high, the internal connections (bonding, etc.) of the rock are forced to fail under the external force. The cracks rapidly develop in all possible directions under the stress, and the micro cracks do not have sufficient time to converge to the main cracking area. Therefore, it requires greater deformation to cause an overall failure of the rock sample. The corresponding macroscopic observation is that the greater the loading rate, the greater the absolute values of the axial strain and the radial strain at the peak point.

3.3 Effects of loading rate on the starting stress of deformation localization

Conventional measurement devices such as strain gauges and extensometers have certain limitations in studying the localization of rock deformation. The application of the 3D-DIC system can properly solve this problem. One advantage of the 3D-DIC system is that virtual strain gauges can be placed at any position on the observation surface. In order to obtain the stress at which the sandstone sample changes from uniform deformation to non-uniform deformation, we have arranged virtual strain gauges inside and outside the localized deformation zone as observed in the snapshots of the principle strain field. The layout of the virtual strain gauges is shown in Fig. 10.

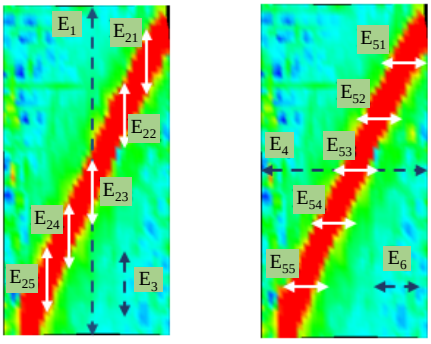

(a) Axial (b) Radial

Fig. 10 Location of virtual strain gauges in observation area

In order to measure the axial strain, we arranged a virtual strain gauge E_1 along the central axis of the specimen, the length of which was the height of the observation area. We placed 5 virtual strain gauges that were uniformly spaced inside the deformation localization zone, denoted as E_{21}, E_{22}, E_{23}, E_{24}, and E_{25} (mean value is denoted as E_2). We also arranged a virtual strain gauge E_3 outside the deformation localization zone, and its length equals the gauges inside the zone.

In order to measure the radial strain, we arranged a virtual strain gauge E_4 along the radial direction in the middle of the specimen, the length of which was the width of the observation area. We placed 5 virtual strain gauges along the radial direction that were uniformly spaced inside the deformation localization zone, denoted as E_{51}, E_{52}, E_{53}, E_{54}, and E_{55} (mean value is denoted as E_5). We also placed a virtual strain gauge E_6 outside the zone with the same length as the gauges inside the zone.

According to the spatial arrangement of the virtual strain gauges, the strain at each gauge position can be derived by the 3D-DIC software, that is, the axial and radial strains can be obtained respectively, as shown in Figs. 11 and 12.

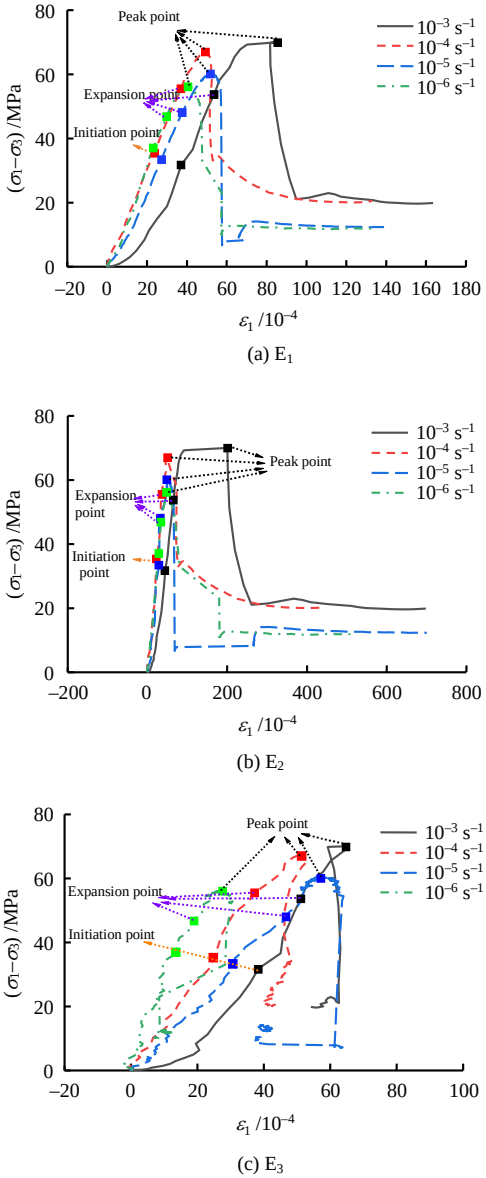

Fig. 11 Plots of deviator stress versus axial strain measured at virtual extensometers (E_1, E_2, E_3) inside and outside the localization zone under different loading rates

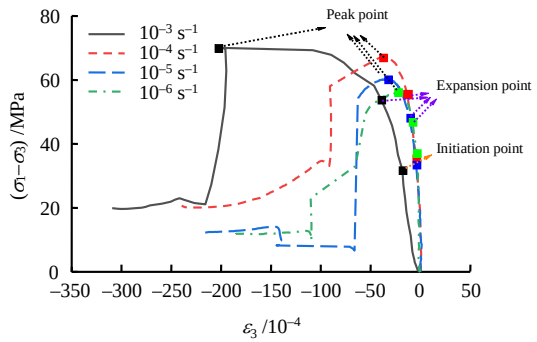

(a) E_4

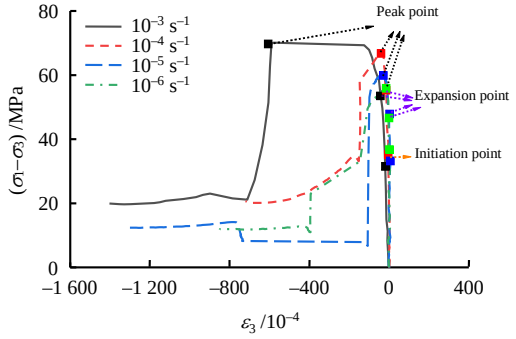

(b) E_5

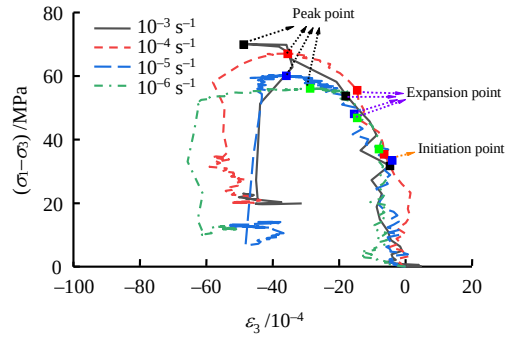

(c) E_6

Fig. 12 Plots of deviator stress versus lateral strain measured at virtual extensometers (E_4, E_5, E_6) inside and outside the localization zone under different loading rates

Figure 11 plots the deviator stress versus the axial strain, where data are collected from the virtual strain gauges at three different positions under different loading rates. According to the change of volumetric strain of rock during loading[27], we have marked the crack initiation point, the expansion point and the peak point on the plot. As shown by the figure, before the peak strength, the axial strains of E_1 and E_2 under different loading rates increase approximately linearly with the increase of stress. It indicates that the rock is still in the elastic stage and no obvious macroscopic cracks appear on the surface. This is consistent with the fact that observed in the snapshots of the strain field.

After the peak arrival, the axial strains of E_1 and E_2 both increase. However, by observing the horizontal axis, the axial strain of plot E_2 that located inside the deformation localization zone shows a much greater increase than that of plot E_1. In contrast, plot E_3 outside the zone shows a slight decrease in axial strain. That is, inelastic unloading appears[17]. This indicates that after the peak arrival, the strains inside and outside the deformation localization zone are very different, and the strain inside the zone is much greater than that outside the zone.

Under the triaxial compression condition, the final failure form of the sample is shear slip. Therefore, in the post-peak stage, the difference between strains inside and outside the deformation localization zone gradually increases with the decrease of stress.

Figure 12 plots the deviator stress versus the radial strain, where the data were collected from the same three different gauges under different loading rates. We used the same criterion to mark each threshold point on the plot. As shown in the figure, similar to the evolution of axial strain, plot E_5 inside the deformation localization zone indicates a sharp increase in radial strain, whereas plot E_6 outside the zone indicates an appearance of inelastic unloading in the radial strain field.

Based on the axial and radial strain shown in Figures 13 and 14, we analyzed the differential results using the axial strains collected by E_1, E_2, and E_3 and the radial strains collected by E_4, E_5, and E_6, respectively. We analyzed the impact of different loading rates on the differentiated axial and radial strain fields.

Figure 13 shows the axial strain difference plot based on the measurements from the three virtual strain gauges at different positions under different loading rates. As shown in Fig. 13, the axial strain difference remains almost constant from the beginning of loading until the peak arrival under different loading rates. Subsequently, the strain differences of E_1–E_2 and E_3–E_2 both increase in the negative direction, whereas the strain difference of E_2–E_3 increases in the positive direction.

Figure 14 shows the radial strain difference plot based on the measurements from the three virtual strain gauges at different positions under different loading rates. Similar to the axial strain difference plot, under different loading rates, the radial strain difference remains almost constant from the beginning of loading until the peak arrival. After that, the radial strain differences of E_4–E_5 and E_6–E_4 both increase in the positive direction, whereas the difference of E_5–E_6 increases in the negative direction.

We plotted the axial and radial strain differences under the same loading rate in order to determine the starting stress to initialize the axial and radial deformation localization. At the beginning of loading, each

difference value is approximately zero. As the loading continues, the curves begin to diverge. The stress corresponding to the jointing point is then the starting stress for deformation localization. During the triaxial compression, if the difference between the three is almost zero or constant at a certain stage, it indicates that the surface deformation of the sample is relatively uniform at that stage. In contrast, if there is a significant difference between the three, it means that the specimen has undergone non-uniform deformation, that is, deformation localization has occurred.

Figures 15 and 16 plot the axial and radial strain differences between the measurements inside and outside the deformation localization zone under a loading rate of 10^{-6} s^{-1}. The horizontal axes show the measured average axial strain from E_1, E_2, and E_3, as well as the measured average radial strain from E_4, E_5, and E_6, respectively.

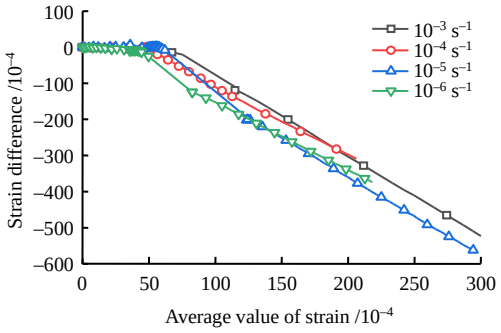

(a) E_1–E_2

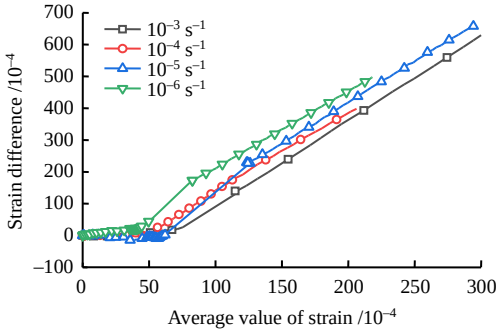

(b) E_2–E_3

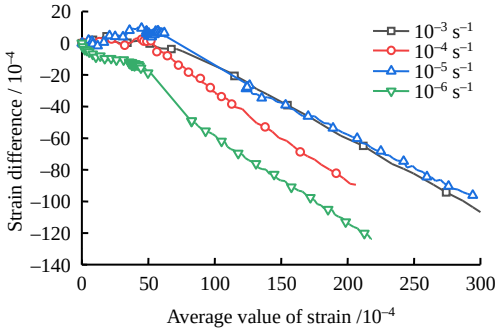

(c) E_3–E_1

Fig. 13 Plots of axial strain difference inside and outside the localized belt

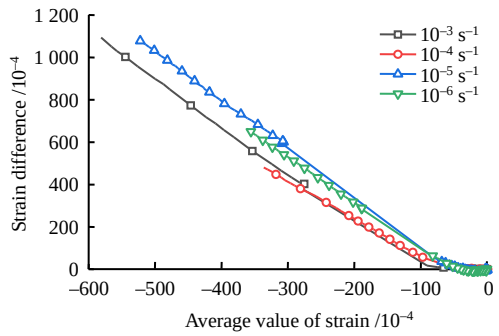

(a) E_4–E_5

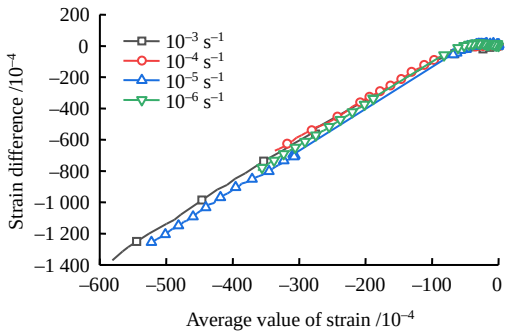

(b) E_5–E_6

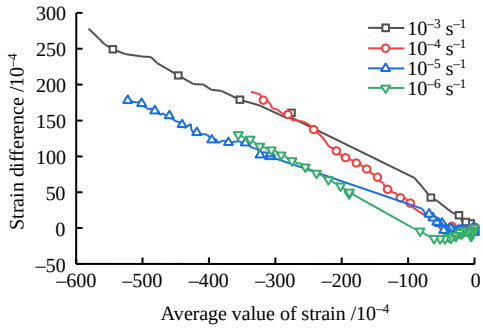

(c) E_6–E_4

Fig. 14 Plots of radial strain difference inside and outside the localized belt

As shown by Figs. 15 and 16, the differences between the three are almost constantly zero from the beginning of loading until the peak arrival. Subsequently, the differences show an obvious divergence, which indicate that the sample has started a non-uniform deformation.

According to the critical point where the divergence starts, the starting stress of the deformation localization can be determined, as well as the ratio between the starting stress and the peak stress to describe a relative level of the starting stress. The results are listed in Table 2. As shown by Table 2, with the increase of loading rate, all the stress thresholds (σ_A, σ_R, and σ_{peak}) and both the ratios (σ_A / σ_{peak} and σ_R / σ_{peak}) increase, and the deformation localization starts earlier. In addition, by comparing the axial and radial strains, the starting time of radial deformation localization is earlier than that of the axial one.

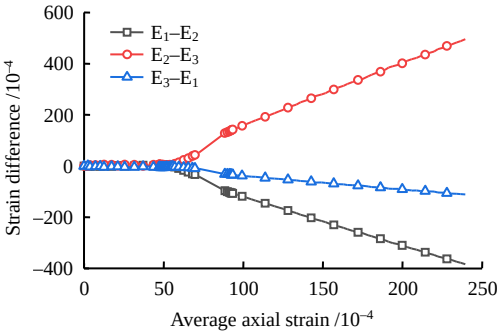

Fig. 15 Plots of axial strain difference inside and outside the deformation localization zone

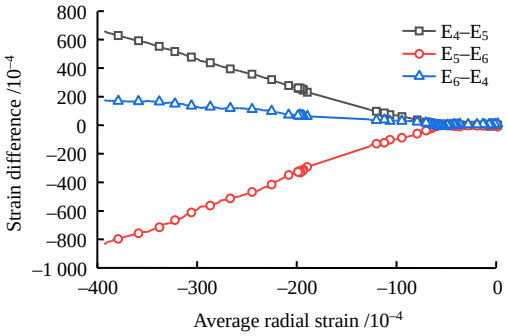

Fig. 16 Plots of radial strain difference inside and outside the deformation localization zone.

Table 2 Stress thresholds at different loading rates

Loading rate C / s^{-1}	Axial starting stress σ_A / MPa	Radial starting stress σ_R / MPa	Peak stress σ_{peak} / MPa	σ_A / σ_{peak} / %	level σ_R / σ_{peak} / %	Stress stage
1×10^{-6}	53.21	54.18	57.81	92.00	93.75	Post-peak
1×10^{-5}	57.51	58.18	61.52	93.53	94.50	Post-peak
1×10^{-4}	65.37	65.79	67.93	96.33	97.00	Post-peak
1×10^{-3}	69.04	68.22	71.04	97.17	96.00	Prior-peak

In order to analyze the effect of loading rate more quantitatively, we use linear regression to fit the data in Table 2, and show the results in Table 3. As shown by the fitting results, the thresholds of starting stress to initialize the deformation localization show a well-fitted linear relationship with the loading rate. In addition, the axial starting stress and its relative stress level are more sensitive to the effects of loading rate compared to the radial ones.

Table 3 Fitting results between the stress threshold and the loading rate

Fitting formula	R^2
$\sigma_A = 5.54C + 86.19$	0.98
$\sigma_R = 4.97C + 83.97$	0.97
$\sigma_{peak} = 4.61C + 85.32$	0.98
$\sigma_A / \sigma_{peak} = 0.02C + 1.03$	0.96
$\sigma_R / \sigma_{peak} = 0.01C + 0.99$	0.67

4 Conclusion

(1) The snapshots of strain fields of the sandstone sample show that the surface deformation is relatively uniform before the peak arrival. When the peak stress is reached, the surface starts to have strain concentration, which rapidly expands after the peak and finally forms a localized deformation zone with an oblique shear distribution.

(2) With the increase of loading rate, the peak strength, elastic modulus, Poisson's ratio, peak axial strain and peak radial strain of the sandstone sample all increase.

(3) The starting stresses to trigger the axial and radial deformation localization (σ_A and σ_R) both increase with the increase of loading rate. When the loading rate increases from 1×10^{-6} s^{-1} to 1×10^{-3} s^{-1}, the axial and radial ratios between the starting stress and the peak stress (σ_A / σ_{peak} and σ_R / σ_{peak}) change from 92.00 % and 93.75% after the peak, to 97.17% and 96.00% before the peak, respectively. The stress thresholds of deformation localization show a well-fitted linear relationship with the loading rate.

References

[1] MOGI K. Source locations of elastic shocks in the fracturing processes in rocks[J]. Bulletin of the Earthquake Research Institute, 1968, 46(Suppl.): 1103–1125.

[2] HU Ming-ming, ZHOU Hui, ZHANG Yong-hui, et al. Analysis of acoustic property of sandstone under uniaxial loading[J]. Rock and Soil Mechanics, 2018, 39(12): 4468–4474.

[3] WU L X, LIU S J, WU Y H, et al. Changes in IR with rock deformation[J]. International Journal of Rock Mechanics and Mining Sciences, 2002, 39(6): 825–831.

[4] SONG Yi-min, XING Tong-zhen, DENG Lin-lin, et al. Experimental study on rock deformation field evolution under different loading rates[J]. Rock and Soil Mechanics, 2017, 38(10): 2773–2779.

[5] DONG Xi-hao, YANG Geng-she, TIAN Jun-feng, et al. Characteristics of deformation properties of frozen sandstone under lateral unloading condition[J]. Rock and Soil Mechanics, 2018, 39(7): 2518–2526.

[6] YIN Xiao-tao, GE Xiu-run, LI Chun-guang, et al. Effect

of loading rate on rock material mechanical behavior[J]. Chinese Journal of Rock Mechanics and Engineering, 2010, 29(Suppl.1): 2610–2615.

[7] WANG Xue-bin. Influence of loading rate on the deformation characteristics of rock samples[J]. Rock and Soil Mechanics, 2008, 29(2): 353–358.

[8] WANG Jie, GONG Jing-wei, ZHAO Ze-yin. Research on the position, direction and early warning application of strain localization of rock specimen under uniaxial compression[J]. Rock and Soil Mechanics, 2018, 39(Suppl.2): 186–194.

[9] SUN Qi, YAO Nian-xi, ZHANG Shu-kun, et al. Study on deformation localization of marble after freeze-thaw corrosion[J]. Journal of Underground Space and Engineering, 2020, 16(1): 97–105.

[10] LI Shu-cai, SUN Chao-qun, XU Zhen-hao, et al. Numerical simulation study on deformation localization of defective rock based on meshless method[J]. Rock and Soil Mechanics, 2016, 37(Suppl.1): 530–536.

[11] TUONG L N, STEPHEN A H, PIERRE V, et al. Fracture mechanisms in soft rock: identification and quantification of evolving displacement discontinuities by extended digital image correlation[J]. Tectonophysics, 2011, 503(1-2): 117–128.

[12] ZHAO Cheng, TIAN Jia-shen, SONG Tian-hao, et al. Study on crack propagation and damage evolution characteristics of rock based on global strain field analysis under uniaxial compression[J]. Chinese Journal of Rock Mechanics and Engineering, 2015, 34(4): 763–769.

[13] DEWERS T A, ISSEN K A, HOLCOMB D J, et al. Strain localization and elastic-plastic coupling during deformation of porous sandstone[J]. International Journal of Rock Mechanics and Mining Sciences, 2017, 98(10): 167–180.

[14] BÉSUELLE P, DESRUES J, RAYNAUD S. Experimental characterization of the localization phenomenon inside a Vosges sandstone in a triaxial cell[J]. International Journal of Rock MecSciences, 2000, 37(8): 1223–1237.

[15] MUNOZ H, TAHERI A, CHANDA E K. Pre-peak and post-peak rock strain characteristics during uniaxial compression by 3D digital image correlation[J]. Rock Mechanics and Rock Engineering, 2016, 49(7): 2541–2554.

[16] DAUTRIAT J, BORNERT M, GLAND N, et al. Localized deformation induced by heterogeneities in porous carbonate analyzed by multi-scale digital image correlation[J]. Tectonophysics, 2011, 503(1-2): 100–116.

[17] YANG Ge, CAI Zong-xi, ZHANG Xiao-chuan, et al. An experimental investigation on the damage of granite under uniaxial tension by using a digital image correlation method[J]. Optics and Lasers in Engineering, 2015, 73(10): 46–52.

[18] ALIABADIAN Z, ZHAO G F, RUSSELL A R. Crack development in transversely isotropic sandstone discs subjected to Brazilian tests observed using digital image correlation[J]. International Journal of Rock Mechanics and Mining Sciences, 2019, 119(7): 211–221.

[19] SHARAFIFISAFA M, SHEN Lu-ming, XU Qing-feng. Characterization of mechanical behaviour of 3D printed rock-like material with digital image correlation[J]. International Journal of Rock Mechanics and Mining Sciences, 2018, 112(12): 122–138.

[20] HUANG Zheng, TU Yong-ming, MENG Shao-ping, et al. Experimental study on shear deformation of reinforced concrete beams using digital image correlation[J]. Engineering Structures, 2019, 181(4): 670–698.

[21] TANG Y, OKUBO S, XU J, et al. Progressive failure behaviors and crack evolution of rocks under triaxial compression by 3D digital image correlation[J]. Engineering Geology, 2019, 249(1): 172–185.

[22] ZHOU X P, LIAN Y J, WONG L N Y, et al. Understanding the fracture behavior of brittle and ductile multi-flawed rocks by uniaxial loading by digital image correlation[J]. Engineering Fracture Mechanics, 2018, 199(8): 438–460.

[23] XING H Z, ZHANG Q B, RUAN D, et al. Full-field measurement and fracture characterizations of rocks under dynamic loads using high-speed three-dimensional digital image correlation[J]. International Journal of Impact Engineering, 2018, 113(3): 61–72.

[24] YANG Xiao-bin, HAN Xin-xing, WANG Xiao-yao, et al. Displacement evolution of rock deformation localization zone under equal amplitude cyclic loading[J]. Journal of China Coal Society, 2019, 44(4): 1041–1048.

[25] WANG Xue-bin, HOU Wen-teng, PAN Yi-shan, et al. Experiments of strain localization processes of coal specimens in uniaxial compression based on the digital image correlation method[J]. Journal of China Coal Society, 2018, 43(4): 984–992.

[26] SEISUKE Okubo, TANG Yang, XU Jiang, et al.

Improvement and application of visual triaxial compression servo control test system[J]. Chinese Journal of Rock Mechanics and Engineering, 2017, 36(Suppl.1): 3351–3358.

[27] SEISUKE Okubo, TANG Yang, XU Jiang, et al. Application of 3D-DIC system in rock mechanic test[J]. Rock and Soil Mechanics, 2019, 40(8): 3263–3273.

[28] LIANG Chang-yu, LI Xiao, WANG Sheng-xing, et al. Experimental study on rate dependence and energy mechanism of stress-strain characteristics of rock under uniaxial compression[J]. Chinese Journal of Rock Mechanics and Engineering, 2012, 31(9): 1830–1838.

[29] SU Cheng-dong, LI Huai-zhen, ZHANG Sheng, et al. Experimental investigation on effect of strain rate on mechanical characteristics of marble[J]. Chinese Journal of Rock Mechanics and Engineering, 2013, 32(5): 943–950.

[30] YANG Shi-jiao, ZENG Sheng, WANG He-long. Experimental study on mechanical effects of loading rate on limestone[J]. Chinese Journal of Geotechnical Engineering, 2005, 27(7): 786–788.

[31] WANG Li-min, XU Dun-shan, LIU Chang-lei. Study on the influence of loading rate on rock failure[J]. Shandong Coal Science and Technology, 2013(2): 126–127.

[32] ZHOU Hui, YANG Yan-shuang, XIAO Hai-bin, et al. Loading rate effect of uniaxial tensile strength characteristics of hard and brittle marbles——test characteristics and mechanism[J]. Chinese Journal of Rock Mechanics and Engineering, 2013, 32(9): 1868–1875.